International Journal of Coal Science & Technology (2022) 9:19
https://doi.org/10.1007/s40789-022-00479-z

RESEARCH

Failure analysis and control technology of intersections of large-scale variable cross-section roadways in deep soft rock

Shengrong Xie[1] · Yiyi Wu[1] · Dongdong Chen[1] · Ruipeng Liu[1] · Xintao Han[2] · Qiucheng Ye[1]

Received: 6 July 2021 / Accepted: 17 January 2022

Abstract

In deep underground mining, achieving stable support for roadways along with long service life is critical and the complex geological environment at such depths frequently presents a major challenge. Owing to the coupling action of multiple factors such as deep high stress, adjacent faults, cross-layer design, weak lithology, broken surrounding rock, variable cross-sections, wide sections up to 9.9 m, and clusters of nearby chambers, there was severe deformation and breakdown in the No. 10 intersection of the roadway of large-scale variable cross-section at the − 760 m level in a coal mine. As there are insufficient examples in engineering methods pertaining to the geological environment described above, the numerical calculation model was oversimplified and support theory underdeveloped; therefore, it is imperative to develop an effective support system for the stability and sustenance of deep roadways. In this study, a quantitative analysis of the geological environment of the roadway through field observations, borehole-scoping, and ground stress testing is carried out to establish the FLAC 3D variable cross-section crossing roadway model. This model is combined with the strain softening constitutive (surrounding rock) and Mohr–Coulomb constitutive (other deep rock formations) models to construct a compression arch mechanical model for deep soft rock, based on the quadratic parabolic Mohr criterion. An integrated control technology of bolting and grouting that is mainly composed of a high-strength hollow grouting cable bolt equipped with modified cement grouting materials and a high-elongation cable bolt is developed by analyzing the strengthening properties of the surrounding rock before and after bolting, based on the Heok-Brown criterion. As a result of on-site practice, the following conclusions are drawn: (1) The plastic zone of the roof of the cross roadway is approximately 6 m deep in this environment, the tectonic stress is nearly 30 MPa, and the surrounding rock is severely fractured. (2) The deformation of the roadway progressively increases from small to large cross-sections, almost doubling at the largest cross-section. The plastic zone is concentrated at the top plate and shoulder and decreases progressively from the two sides to the bottom corner. The range of stress concentration at the sides of the intersection roadway close to the passageway is wider and higher. (3) The 7 m-thick reinforced compression arch constructed under the strengthening support scheme has a bearing capacity enhanced by 1.8 to 2.3 times and increase in thickness of the bearing structure by 1.76 times as compared to the original scheme. (4) The increase in the mechanical parameters c and φ of the surrounding rock after anchoring causes a significant increase in σ_t; the pulling force of the cable bolt beneath the new grouting material is more than twice that of ordinary cement grout, and according to the test, the supporting stress field shows that the 7.24 m surrounding rock is compacted and strengthened in addition to providing a strong foundation for the bolt (cable). On-site monitoring shows that the 60-days convergence is less than 30 mm, indicating that the stability control of the roadway is successful.

Keywords Deep soft rock · Variable cross-section · Roadway intersection · Bolting-grouting integration · New grouting material

1 Introduction

With the exhaustion of shallow coal resources, coal mining in east-central China has shifted to deeper realms (Cai and Brown 2017; Chen et al. 2019). Deep ground stress is high, mining has a considerable influence, surrounding

✉ Dongdong Chen
chendongbcg@163.com

[1] School of Energy and Mining Engineering, China University of Mining and Technology, Beijing, Beijing 100083, China

[2] Mine Safety Technology Branch of China Coal Research Institute, Beijing 100013, China

Published online: 30 March 2022

rock deformation has great mobility, expansion, and impact; hence, adequate support of roadways is becoming increasingly problematic (Liu 2011; Fairhurst 2017; Xie et al. 2018). A long service life and high stability are essential requirements in the development of roadways. The environment at great depths is unique owing to the complicated geological conditions (Wagner 2019; Ranjith et al. 2017; Xue et al. 2020). The No. 10 intersection examined in this study includes a portion of the roadway of width 9.89 m with loose and fractured surrounding rock that was seriously damaged by strong tectonic stress at that depth and traverses uneven strata. Consequently, traditional anchor support is inadequate to withstand the significant deformation damage that occurs in practice (Pan et al. 2017).

Many academics have carried out thorough studies on the control and design of surrounding rocks to address the challenge of providing an appropriate support system for deep roadways in complicated geological settings. Tian et al. (2020) suggested a support system for deep soft rock submerged roads based on high-strength anchoring, a high-stiffness spraying layer to prevent water, and deep and shallow hole grouting to rebuild the damaged surrounding rock. Xie et al. (2019) suggested a complete control approach for deep large-section chambers such as strong bolt (cable) support, thick-walled reinforced concrete pouring, and full-section pressure-regulating grouting behind the walls. Kang et al. (2014) developed a novel form of an integrated support system and floor monitoring technique to prevent and manage the weak floor of a deep roadway. Huang, Li, and Zhang et al. utilized a novel steel pipe concrete reinforced support that successfully suppressed serious deformation of deep roadways (Huang et al. 2018; Li et al. 2020; Zhang et al. 2018). Wang et al. (2017) investigated the damage and control mechanisms of deep soft rock roadways and proposed the idea of "high-strength, integrity, and pressure-relief". Yang et al. (2017) used a combination technique of "bolt-cable-mesh-shotcrete + shell" to successfully control the deformation of a deep soft rock roadway. Wang et al. (2015) presented a dynamic damage intrinsic model to evaluate the elastic rebound and shear expansion deformation of the surrounding rock during the unloading process and addressed the pre-peak and post-peak phases in their theory of rock damage in deep roadways. Huang and Li et al. performed a numerical simulation of deep rock cutting and fracture patterns (Huang et al. 2016; Li et al. 2016). Peng et al. (2018) in their study of the structural damage process of deep roadways, reported that horizontal stress had a significant impact on the stability of the surrounding rock and developed a multi-stage support system based on the structural features of the roadway bearing. Shreedharan and Kulatilake (2015) employed the 3DEC discrete element technique to assess the stability of a deep coal mine roadway under various sections and support bodies in their numerical simulation of a deep roadway support. Wang et al. (2020) utilized ABAQUS to create a finite element model under the original support design, suggested a zoned bolt-grouting reinforcement technology, and numerically tested its support impact. Using self-developed random non-destructive testing methodologies and equipment, Zhang et al. (2017) suggested an early warning system for the integrity of the roadway envelope based on anchor axial load detection.

The research above provided a sound theoretical and engineering foundation for controlling surrounding rocks in deep roadways; however, a majority of the studies focus on a single geological or roadway attribute, such as soft rock, fractured surrounding rock, flooded roadways, or large section chambers, rather than examining the efficient sustenance of deep roadways under the influence of many varying factors. In addition, numerical simulations using a single intrinsic relationship ignore the difference in mechanics between a tunnel envelope and undisturbed rock formations. Moreover, the existing amount of research on the support of variable-section roadways is relatively small, and the numerical modeling of variable-section roadways under inclined coal rock layers is over-simplified, which affects the accuracy of the results. The lack of a theoretical model of bolt (cable) support based on soft rock environment in deep roadway results in inappropriate selection of support materials. The present cement slurry-based grouting material has a large number of flaws; therefore, it is difficult to ensure grouting action in deep roadways.

The intersection of the − 760 m level No. 10 roadway in a coal mine is the subject of research in this study, and the coupling impact of many variables such as deep high stress, adjacent faults and interlayer arrangement, weak lithology, fractured surrounding rocks, varied cross-sections, large cross-sections up to 9.9 m wide, and clusters of neighboring chambers were examined as the reasons for its deformation and collapse. Field observation, borehole-scoping, and in-situ stress testing were used to determine the geomechanical characteristics of the roadway. The strain-softening features of the surrounding rock in the post-peak stage were modeled and studied, and the internal friction angle and cohesive force weakening law of the rock were deduced. Curve fitting of the triaxial test was performed using FLAC 3D; the inverted parameters were applied to the FLAC 3D variable cross-section roadway model to achieve the coupling of the surrounding rock strain softening and Mohr–Coulomb constitutive model, to effectively analyze the force and deformation characteristics of the roadway intersection. For support design analysis, a thick reinforced compression arch mechanical model, based on the quadratic parabolic Mohr strength criteria, was developed for the surrounding conditions of deep soft rock, and the strengthening support scheme with the action path of "deep hole grouting and anchoring → reinforcement of broken surrounding

rock → mutual cementation into the arch → realization of self-supporting surrounding rock" was proposed, i.e., the anchor injection integrated the support technology based on a hollow grouting anchor cable equipped with a modified grouting material. Simultaneously, the impact of changes in the parameters of the surrounding rock mechanics before and after bolting and grouting on strength was evaluated using the Heok-Brown criteria, and a supporting prestress field was constructed to simulate and validate the plan. The roadway was monitored for displacement and borehole-scoping following on-site construction, and it was observed that the control effect on the stability of the surrounding rock was good, providing a theoretical direction and engineering reference for roadway support under the arduous circumstances at great depths.

2 Engineering background

2.1 Geological profile

The mine studied is equipped with a fully mechanized top-coal caving face that is mainly used in the No. 3 coal seam of the Shanxi Formation in the Qinshui Coalfield, and the designed annual output reaches 3.0 Mt/a. The bottom yard of the air intake shaft is located under the No. 3 coal seam with a buried depth of approximately 760 m. The strike of the coal and rock strata is north high and south low by 12°, and west high and east low by 5°. The rock layers traversed by the roadway at the bottom of the shaft are sandy mudstone, thin mudstone, and sandy mudstone interbeds, where the rock is broken. The overall stability is poor and a bedding of V-level unstable rock mass (It refers to broken soft rock with basic quality index BQ ≤ 250) is developed that leads to frequent roof fall in roadway excavation. After the implementation of the original support scheme, the accidents of large deformation, roof fall and slope still occur in the roadway, and the original support scheme can not effectively control the surrounding rock deformation (the original support scheme and failure condition will be shown in detail below). A comprehensive histogram of the strata is shown in Fig. 1.

2.2 Engineering characteristics

The largest cross-section at the No. 10 intersection is formed by the intersection of people and vehicle parking chambers (referred to as parking chambers), and pedestrian and vehicle parking chamber passages (referred to as chamber passages). In view of the geological background of deep high stress, practical conditions of the concentrated chamber group, and large cross-section at the intersection, a comprehensive site observation of the deformation due to the stress environment, characteristics of the surrounding rock, cross-section of the intersection, and construction technology yielded the following characteristics of the project:

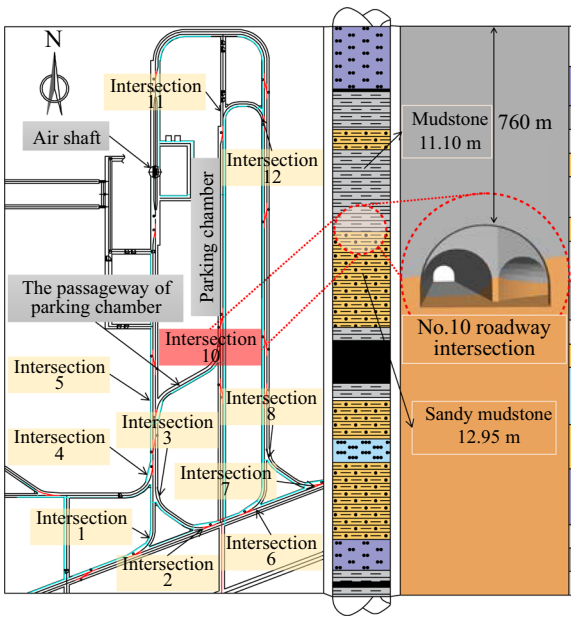

Rock stratum	Thickness /m	Lithology description
Medium sandstone	8.70	Gray, medium to thick laminated, feldspar, quartz dominant, uniformly laminated, well sorted, well rounded
No.1 coal seam	0.35	Black coal line
Mudstone	5.15	Gray-black, medium-thick laminated, brittle, flat fracture
Sandy mudstone	2.75	Light gray-black, medium-thick laminate, flatter fracture
Mudstone	11.10	Light gray-black, medium-thick laminate, brittle, shell-like fracture
Sandy sudstone	12.95	Light gray-black, medium-thick lamellar, jagged fracture
Mudstone	1.80	Gray-black, medium-thick laminated, brittle, shell-like fracture, containing plant fossils
No.3 coal seam	5.80	Black, bright coal mainly, dark coal second, semi-bright coal
Mudstone	2.35	Dark gray-black, lumpy, flat fracture
Sandy mudstone	5.20	Light gray-black, medium-thick laminated, flat fracture
Fine sandstone	3.20	Gray, thickly laminated, quartz dominant, feldspar secondary, with coal dust, mica, with muddy streaks, sorted
Sandy mudstone	10.45	Dark gray-black, blocky, brittle, flat fracture, containing plant fossils
Medium sandstone	4.20	Gray, medium-thick laminated, feldspar, quartz dominated, three vertical fissures of 0.4 m in length developed
Mudstone	1.55	Dark gray-black, lumpy, brittle, flat fracture
No.5 coal seam	0.75	Black coal line
Mudstone	1.30	Dark gray-black, lumpy, brittle, flat fracture

Fig. 1 Comprehensive histogram of the stratum at the intersection of the roadway

2.2.1 Intersections with a concentrated arrangement resulting in stress concentration

As shown in Figs. 2, 11, roadway intersections connect three transport roadways near the − 760 m shaft bottom yard in the Nanfeng work area, that form a centralized chamber group along with pipes, pedestrian parking chambers, and horsehead gates. The roof mudstone of the chamber group is not strong and is rich in clay minerals such as a mixed layer of illite/montmorillonite and kaolinite. This makes the surrounding rock soft, strong-swelling, easily attacked by chemicals, and readily weathered (Kang et al. 2015; Yu et al. 2020). In this environment, densely distributed intersections lead to overlapping stresses. At the largest cross-section at the No. 10 intersection, the range of stress concentration is substantial and the peak stress reaches more than twice the original rock stress (This is the result of the later numerical calculation, which is shown below). This directly causes severe deformation of the surrounding rock at the intersection giving rise to serious cracking of the shotcrete layer in the roadway.

2.2.2 Poor surrounding rock lithology owing to the proximity of faults and placement through layers

As shown in Figs. 3, 4, the south side of the No. 10 intersection is near the normal fault CF47, where the ground stress is dominated by tectonic stress, the surrounding rock strength is low, and integrity is poor. Moreover, the depth of the roadway is large and the surrounding rock of the nearby roadway is broken to some extent, making the

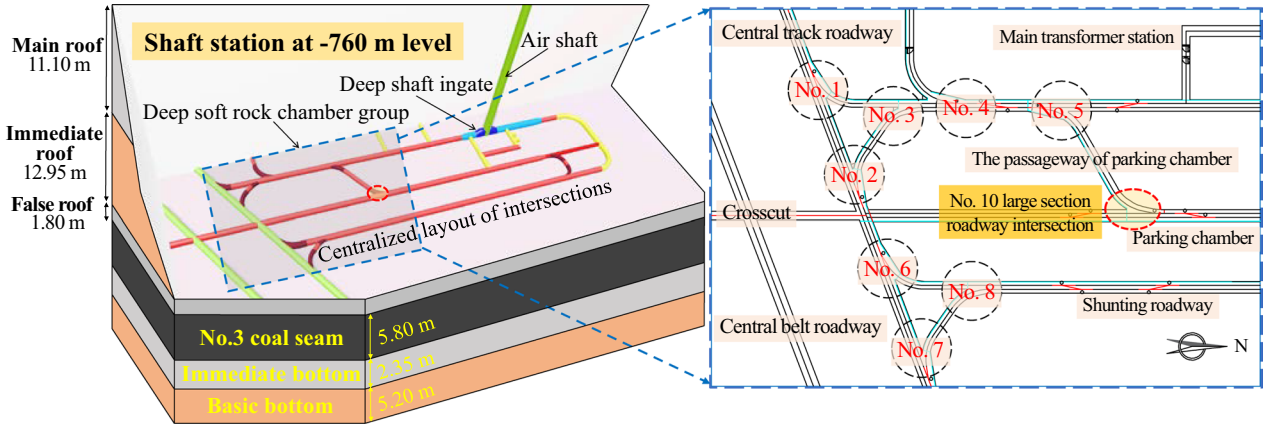

Fig. 2 Location map of all roadway intersections

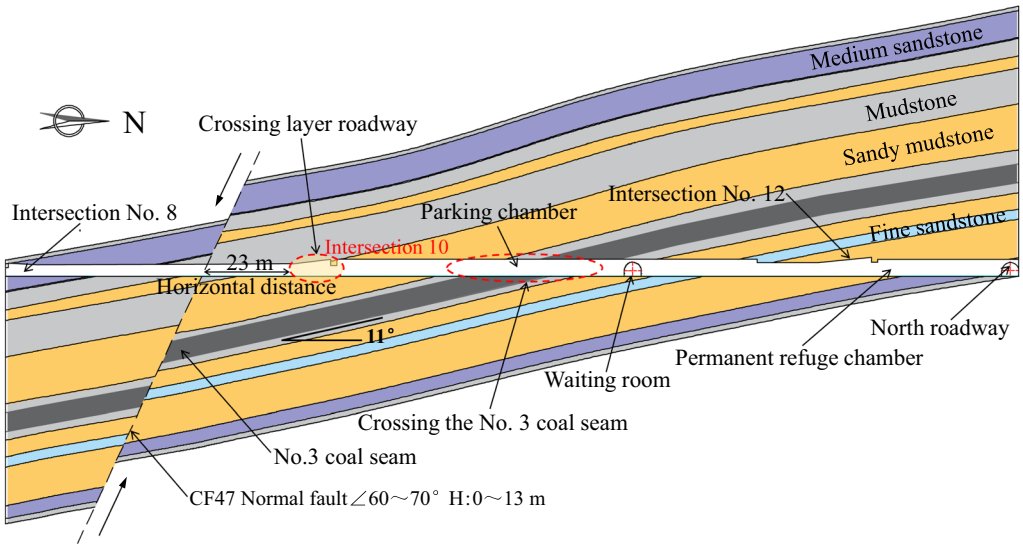

Fig. 3 Stratigraphic profile at the No. 10 intersection

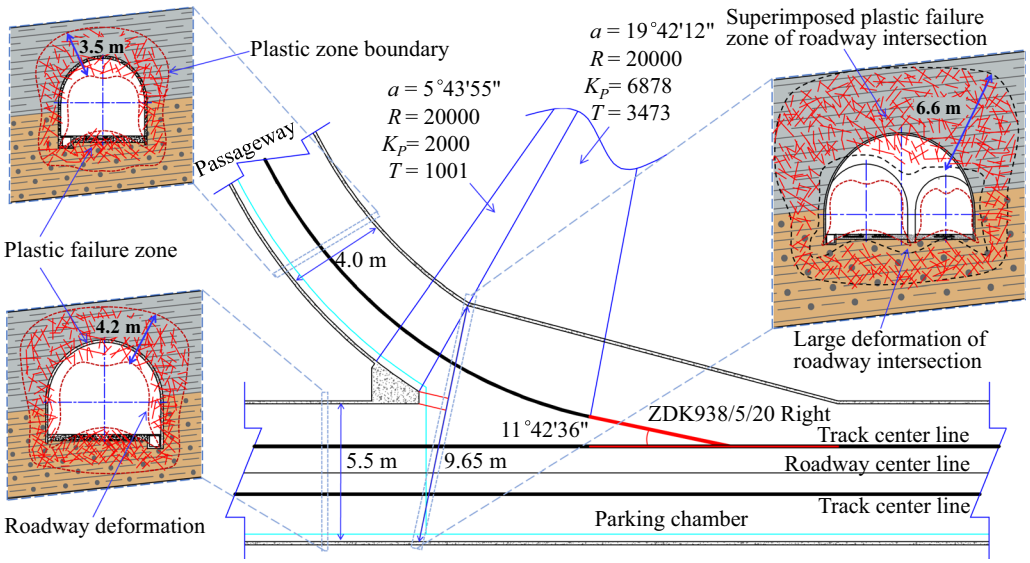

Fig. 4 Schematic of the plastic zone of each section at the No. 10 intersection

support inadequate (Zhang et al. 2019). The intersection crosses over the junction of the layers of mudstone and sandy mudstone with the bottom of the roadway as the datum, and is almost 0.7–3.0 m from the datum. Therefore, the No. 10 intersection through the layer triggers the plastic zone in each part to be at a higher level thus increasing the volume of the plastic zone, which directly causes the surrounding rock to be loose and broken.

2.2.3 A large cross-sectional area of the intersection extending the range of disturbance of the surrounding rock

The above picture shows the field measurement results of plastic failure zone in the early stage of the original support design, and the No.10 intersection is a large section chamber with a tunneling width of 9.89 m. The rock body is in a long-term rheological deformation process; the plastic zone is more developed and creates a wide range of superimposed plastic zones around the junction due to the vast burial depth, enormous section, and fractured surrounding rock (Tan et al. 2019). Further, the strength and integrity of the surrounding rock at the intersection are poor; hence, the stress causes it to reach the plastic yield condition, leading to plastic flow on both sides of the roadway, as well as shear yield and tensile failure in the region. The actual damage at the comprehensive site intersection, under the effect of strong disturbances, results in overall deformation and instability, and causes chain damage to the cavity group in severe cases.

2.2.4 Difficult construction and maintenance of large cross-sectional intersections.

The occurrence of rib spalling and roof falling is frequent in the process of digging and excavating; the roadway is poorly shaped, especially the No. 10 intersection that is 9.9 m wide and up to 6.5 m high. Moreover, the shotcrete layer of the major support section contains cracks and falling blocks; thus, breaking and falling off of the wall takes place to the extent of different degrees during roadway maintenance.

3 Damage deformation analysis

On account of the field working conditions of the No. 10 intersection, large deformation of the roadway, and broken surrounding rock, the methods of drilling peek, in-situ stress measurement, and numerical simulation were used to analyze the surrounding rock plastic zone, roof displacement, and stress conditions.

3.1 Drilling peek detection

Drilling peeking at intersection 10 is shown in Fig. 5: (1) The surrounding rock from 0–0.4 m was relatively broken with intense fissures. (2) There was loose destruction of the surrounding rock at a depth of 0.4–4.2 m, the open fractures were concentrated in the shallow fracture development area, and cracks were developed intensively within a depth of 4 m. (3) There were a large number of fine original fractures in the slight crack area of 4.2–6.6 m, that reduced from the

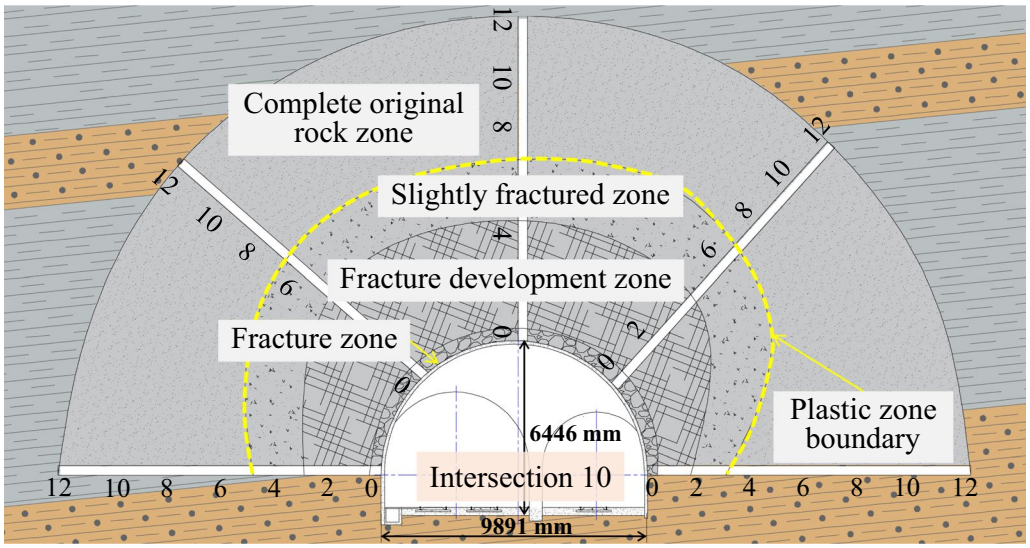

Fig. 5 Schematic of borehole-scoping and zoning failure of the surrounding rock

shallow to deep region. (4) The deep surrounding rock from 6.6–12 m was complete with dense rock formations and no obvious cracks. (5) The degree of breakage was greater in the roof and shoulder of the surrounding rock than that at the side; hence, roof control was the focus of our study.

3.2 In-situ stress measurement

As shown in Fig. 6, an in-situ stress measurement technique based on CSIRO cell was applied to the field measurements at the No. 10 intersection. The average result of the measured point data showed that the ground stress type was $\sigma_H > \sigma_V > \sigma_h$. The maximum principal stress (near the horizontal direction) of the measuring point was nearly 30 MPa and the average ratio of the maximum principal stress to vertical stress was 1.67, which is a state of high tectonic stress. The roof and floor control of the roadway support is particularly important in the case of the in-situ stress field dominated by horizontal stress. The roof of the site was soft mudstone with many broken rock blocks, hence, support was difficult. Therefore, modification and strengthening of the surrounding rock was the key to forming a support system.

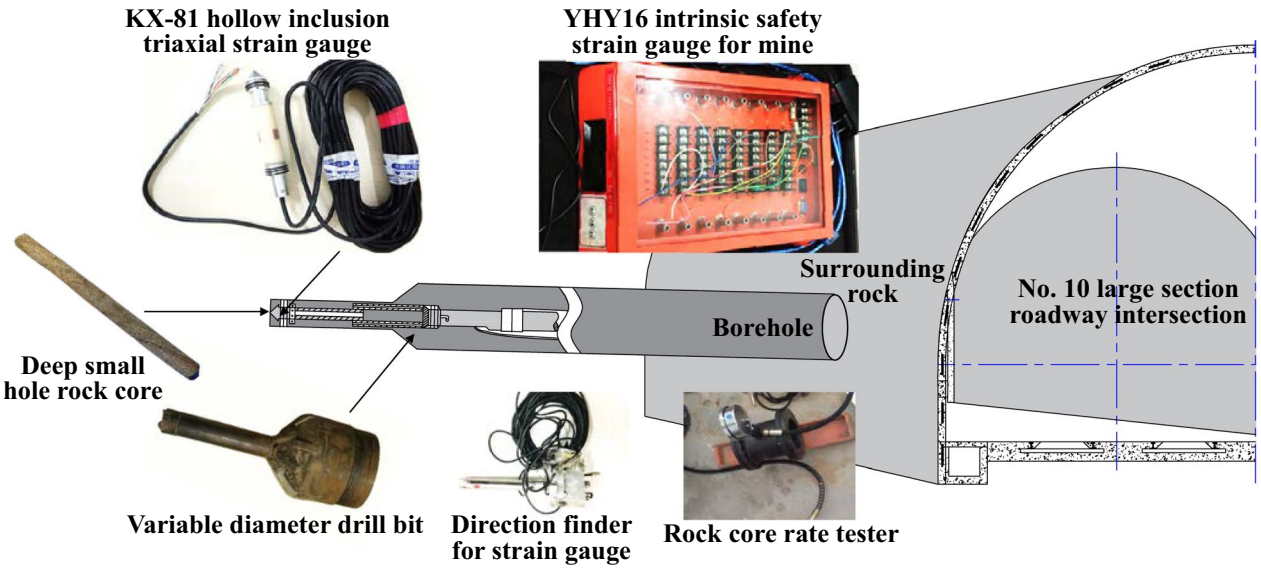

Fig. 6 Schematic of in-situ stress measurement

3.3 Analysis of the failure of the original support scheme

In Fig. 7, the original support scheme consisting of an anchor network cable spray + double-steel-bar ladder beam is shown. After the construction, there was large deformation of the roadway section, sinking and cracking of the roof, roof and rib falling, and failure and falling of bolts (cables). The original supporting bolts (Here is the bolt anchored at the end of the resin cartridge) were 2.4 m long, all of which were in the fracture development concentrated area where they were unable to function; ordinary cable bolts (ordinary cable bolt refers to common cable bolt with 7-core steel strands) were 7.6 m long with large spacing and low elongation. The broken surrounding rock did not allow for an effective anchoring foundation, thus the performance of the anchor cable was inadequate and a stable supporting structure was not formed. Hence, the supporting body failed to exert the self-bearing capacity of the surrounding rock.

3.4 Establishment of FLAC 3D model for the No. 10 intersection

Based on the engineering geological characteristics of the No. 10 intersection, a FLAC 3D model that conformed to the actual condition of the site and showed the crossing form of the roadway to the greatest extent was constructed, and is shown in Fig. 8. The constitutive relationship of the model adopted the Mohr–Coulomb criterion and the rock formation (mudstone and sandy mudstone) was coupled with the strain-softening constitutive relationship at the intersection point to indicate that the strength of the broken rock was mostly its residual strength. According to the experiment on rock mechanics conducted with the rock core taken from the site, the mechanical parameters of the coal and rock strata given in the following Table 1 were adopted for the numerical simulation.

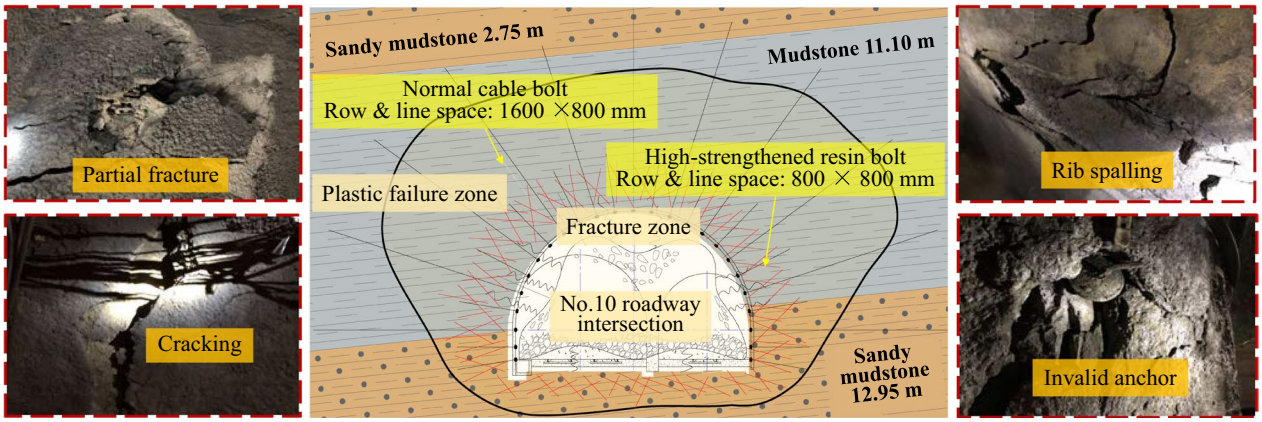

Fig. 7 Schematic of original support scheme and roadway breakdown and deformation

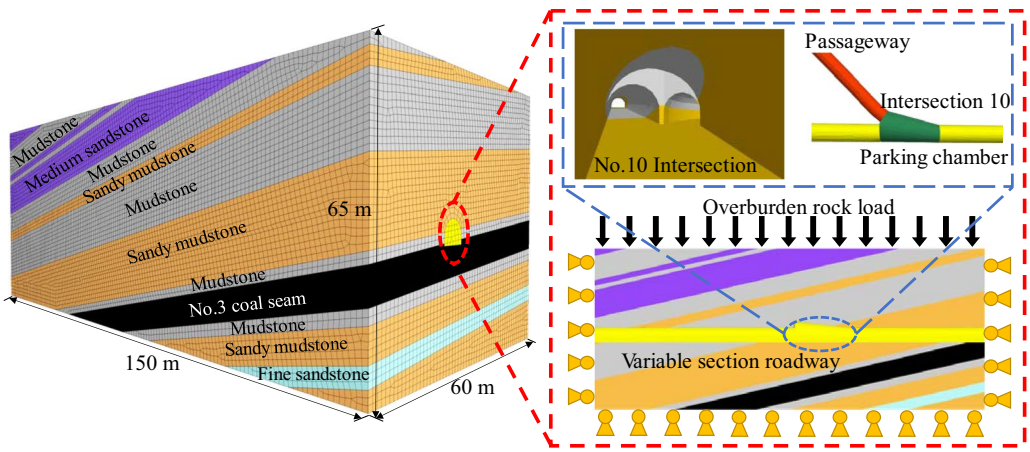

Fig. 8 FLAC 3D numerical model of the No. 10 intersection

Table 1 Parameters of coal and rock mechanics used in numerical simulation

Rock stratum	Average thickness (m)	E (GPa)	K (GPa)	c (MPa)	σ_t (MPa)	φ (°)	γ (kg/m^3)
Medium sandstone	5.55	16.73	10.72	5.54	3.58	37.00	2731
Mudstone	7.65	9.66	7.00	2.83	1.19	32.00	2463
Medium sandstone	1.70	15.50	9.94	5.34	3.45	37.00	2713
Mudstone	1.30	11.34	8.22	2.62	1.12	33.00	2466
Medium sandstone	8.70	15.21	9.75	5.46	3.53	37.00	2801
Mudstone	5.50	8.69	6.30	2.34	1.05	30.00	2414
Sandy mudstone	2.75	12.94	8.63	4.78	2.81	35.00	2567
Mudstone	11.10	9.03	4.80	2.69	1.09	30.00	2453
Sandy mudstone	12.95	13.65	9.10	4.92	3.12	36.00	2646
Mudstone	1.80	10.21	7.40	2.54	1.07	32.00	2429
No. 3 coal seam	5.80	5.20	4.33	1.25	0.82	25.00	1423
Mudstone	2.35	9.46	6.86	2.75	1.13	31.00	2457
Sandy mudstone	5.20	12.30	8.20	4.62	2.80	35.00	2549
Fine sandstone	3.20	23.40	13.93	5.87	3.79	38.00	2815
Sandy mudstone	10.45	13.50	9.00	4.75	2.76	35.00	2606

3.5 Simulation of strain-softening mechanical characteristics

3.5.1 Strain softening mechanical model

The No. 10 intersection is at the junction of 12.95 m sandy mudstone and 11.10 m mudstone. The surrounding rock is quite broken and the softening characteristics of the post-peak are the main factors affecting the deformation and deterioration of weak rocks. Therefore, based on the results of the triaxial compression test of the two types of rocks shown in Fig. 9 (Huang et al. 2014; Lu et al. 2010), an ideal trilinear strain-softening model curve was constructed (Fig. 10) (Kawamoto and Ishizuka 1981). As shown in Fig. 10 of the simplified model, *OA* and *OB* are the pre-peak elastic deformation stages of the rock and the secant of the peak point was used as an approximate replacement, where *l* is the unloading path. After the peak point, the rock enters the strain-softening stage, The slope of the post-peak stage of each triaxial test curve is fitted and calculated, and an oblique line is obtained to represent the post-peak strain softening stage (Alonso et al. 2003; Lee and Pietruszczak 2008), then the average post-peak slope of triaxial test curves with different confining pressure is taken,

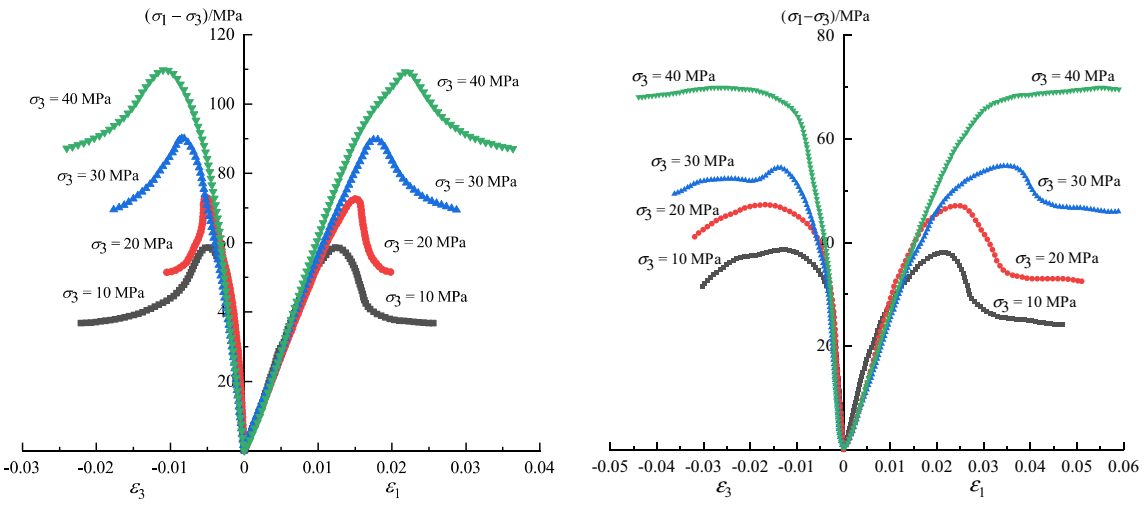

(a) Sandy mudstone (b) Mudstone

Fig. 9 Full stress–strain curves of two types of rocks under different confining pressures in triaxial compression tests

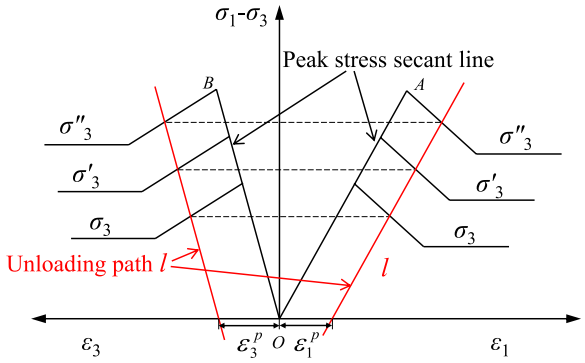

Fig. 10 Post-peak rock strain-softening plastic strain–stress relationship

and a unified post-peak slope is obtained (Yao et al. 2018; Zhang et al. 2008). Assuming that the unloading process is linearly elastic, there is *l*//*OA*, and the same plastic deformation is produced along the unloading path *l* under different confining pressures.

3.5.2 Yield surface of the strain-softening stage of the rock

Owing to the accumulation of the history of plastic deformation of the rock and randomness of the instantaneous stress state, the subsequent yield surface is different from the elastic stage. To record the history of plastic loading of the rock material, the rock was considered to be anisotropic. The strain-softening parameter ε^{ps} was used as the plastic state variable (Lu et al. 2010; Zhang et al. 2008) given by the following formula:

$$\varepsilon^{ps} = \frac{\sqrt{2}}{6}\sqrt{\left(2\varepsilon_1^p - \varepsilon_3^p\right)^2 + \left(\varepsilon_1^p + \varepsilon_3^p\right)^2 + \left(2\varepsilon_3^p - \varepsilon_1^p\right)^2} \quad (1)$$

where ε_1^p and ε_3^p are the principal plastic strain components. Therefore, the subsequent yield surface of the rock after the peak is expressed as

$$f\left(\sigma_1, \sigma_2, \sigma_3, \varepsilon^{ps}\right) = 0 \quad (2)$$

where σ_1 is the first principal stress, σ_2 and σ_3 are the second and third principal stresses, respectively, and $\sigma_2 = \sigma_3$. It was assumed that the stress state at a point in the post-peak strain-softening stage at different ε^{ps} is in the critical state of strength failure, i.e., the Mohr–Coulomb criterion is satisfied.

$$f = \sigma_1 - \sigma_3\frac{1+\sin\varphi'}{1-\sin\varphi'} + 2c'\sqrt{\frac{1+\sin\varphi'}{1-\sin\varphi'}} \quad (3)$$

where the internal friction angle φ at the critical state and the cohesive force c under different ε^{ps} are calculated inversely, and the law of φ and c changing with ε^{ps} of the two types of rocks under study can be obtained simultaneously.

3.5.3 Internal friction angle and weakening law of cohesion

In the strain-softening stage of the rock, the value of the principal stress difference in the rock gradually decreases as the plastic strain increases, and this decreasing trend is reflected in the change of the rock c and φ values. Figure 11 is based on the type (2) (3) to obtain the different

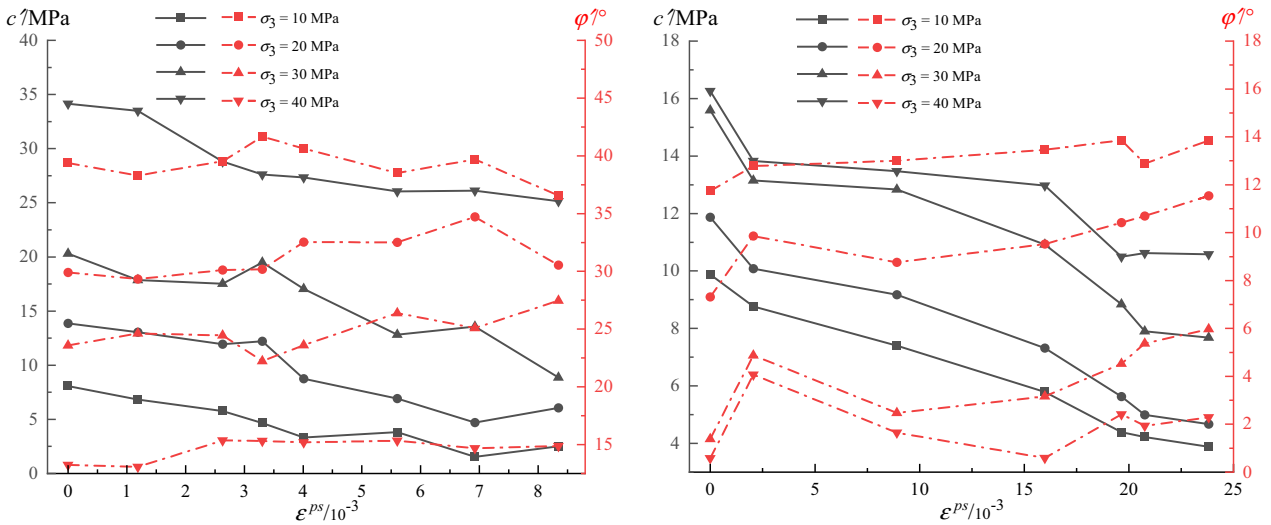

Fig. 11 Curves of the relationship between c', φ', and ε^{ps} under different confining pressures

circumferential pressures c', φ' relationship curve with the ε^{ps}.

By calculating the values of c and φ of the sandy mudstone and the mudstone for 8 groups of different ε^{ps}, the relationship curve was obtained, shown in Fig. 11. Under different confining pressures, the values of the cohesive force c of the two types of rocks gradually decreased with an increase in the strain-softening parameter ε^{ps}, whereas the value of φ remained unchanged during the strain-softening process. The linear equation was fitted by the downward trend of the two types of rocks c and the average gradient of the decrease was obtained (Table 2).

3.5.4 FLAC 3D triaxial test simulation

The modified strain-softening model was embedded into the FLAC program to verify the accuracy of the softening model described above. The standard triaxial test model shown was established in FLAC 3D (Fig. 12). By applying different confining pressures, the stress–strain curves of sandy mudstone and mudstone based on the above softening model were obtained, and the simulation and experimental curves were compared (Fig. 13). The two types of curves were quite consistent proving that the softening model can describe the post-peak mechanical properties of the two types of rocks.

3.6 Analysis of the deformation and force

3.6.1 Analysis of the displacement

The displacement of the roof at the intersection was large as compared to that at both the sides of the roadway, especially at the maximum cross-section where it was nearly double; this indicates that the surrounding rock deformation was acute (Fig. 14). The range of displacement is clear from the three-dimensional cloud map where the maximum displacement at the roof gradually attenuates from the maximum cross-section of the intersection to the front, rear, and

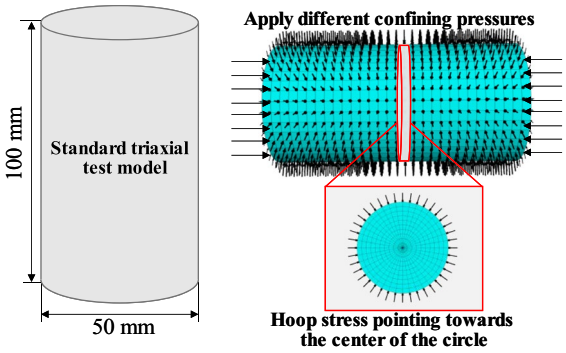

Fig. 12 Model of FLAC 3D triaxial test

right sides of the roadway. The front and rear attenuation range was approximately 40 m, and that at the right side was approximately 10 m. In engineering practice, roof falling disasters occur frequently at the intersection of roadways during tunneling, therefore, it is difficult to control large cross-sections of roadways.

3.6.2 Analysis of plastic zone

The FLAC 3D model of the circumscribed circle of a cross-section of the semi-circular arched roadway at the No. 10 intersection was established. According to the results of the in-situ stress test, a vertical stress of 18 MPa and horizontal stress with the lateral pressure coefficient of 1.67 were applied to it. As shown in Fig. 15, the plastic zone of the No. 10 cross roadway was 4.20–6.61 m deep into the surrounding rock. The range of the plastic zone between the roof and shoulder was wide and reduced gradually from the two sides to the bottom corner. The overall shape of the plastic zone was asymmetric because the roadway passed through the interbedded mudstone and sandy mudstone. The average depth of the plastic zone at the right roof was greater than that at the left roof. The worst case must be considered in devising a support system; therefore, the effective anchorage

Table 2 Parameters of cohesion reduction trend fitting curve

Lithology	Confining pressure (MPa)	Straight line equation	Correlation coefficient R^2	Average gradient	Average correlation coefficient R^2
Sandy mudstone	10	$y=-0.7304x+7.4885$	0.8731	−1.0615	0.8569
	20	$y=-1.1686x+14.358$	0.8871		
	30	$y=-1.2472x+20.927$	0.8368		
	40	$y=-1.0996x+32.983$	0.8307		
Mudstone	10	$y=-0.2513x+9.606$	0.9886	−0.2658	0.9418
	20	$y=-0.2892x+11.444$	0.9709		
	30	$y=-0.3085x+15.008$	0.9377		
	40	$y=-0.214x+15.393$	0.87		

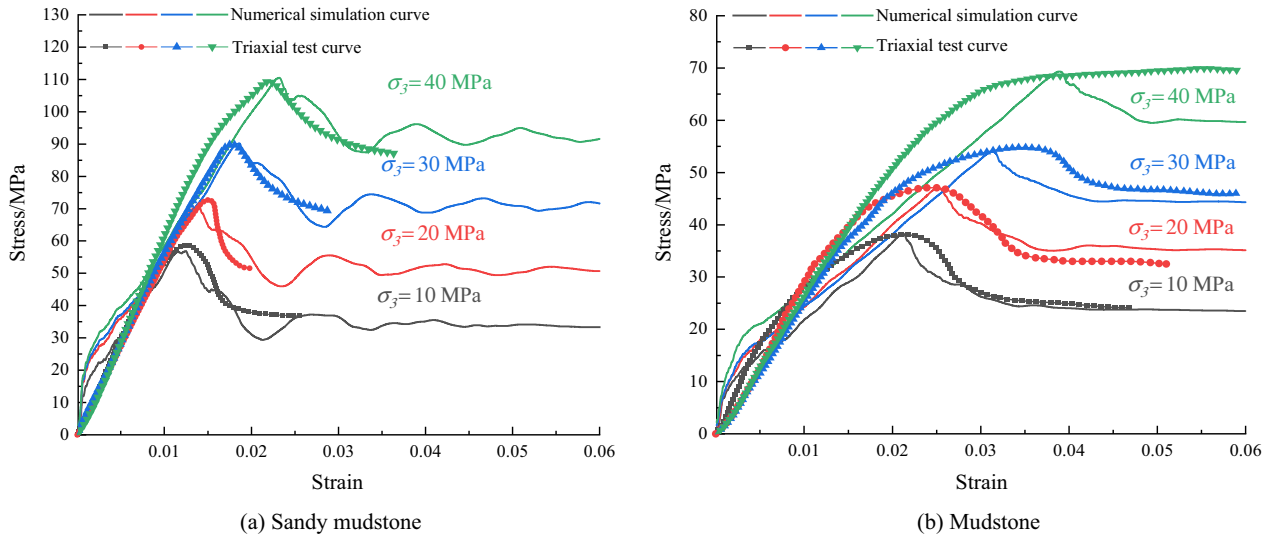

Fig. 13 Fitting graph of numerical simulation and experimental data

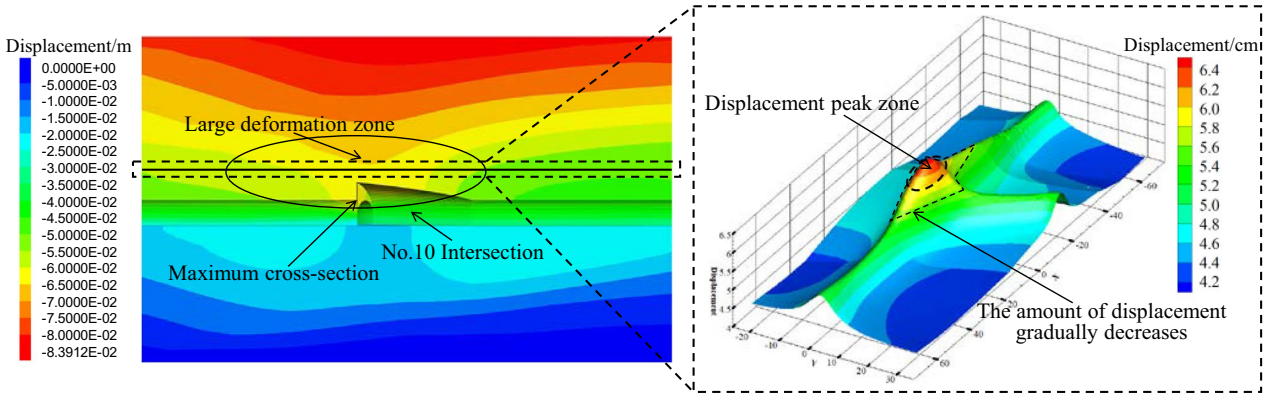

Fig. 14 Vertical displacement cloud of roadway intersection

length of the strengthening support must be greater than the maximum depth of the plastic zone (6.61 m) and mainly, the roof and shoulders must be controlled.

3.6.3 Analysis of the stress

It is evident from the three-dimensional stress equipotential surface shown in Fig. 16 that the value of the stress, concentration coefficient, and range of the roadway intersection are considerably increased. Here, the maximum stress was 42 MPa, which was 2.3 times the original rock stress of 18 MPa. The stress concentration coefficient at the largest section was greater than 2, indicating a strong degree of stress concentration. The stress slice of the entire section of the crossing roadway shows that the stress concentration area ranges from 5.65–6.85 m; the range and degree of stress concentration are higher on the side of the passageway near the roadway intersection.

4 Research on the integration of bolting and grouting support

4.1 Construction and analysis of thick reinforced compression arch structure

In view of the characteristics of the large deformation of the surrounding rock and sizeable range of plastic zones at the No. 10 intersection, and the rapid failure of ordinary support schemes, the design of the strengthening support plan must meet the mechanical properties that can effectively deep anchor and reinforce the plastic zone. A strengthening support scheme with hollow grouting anchor cables

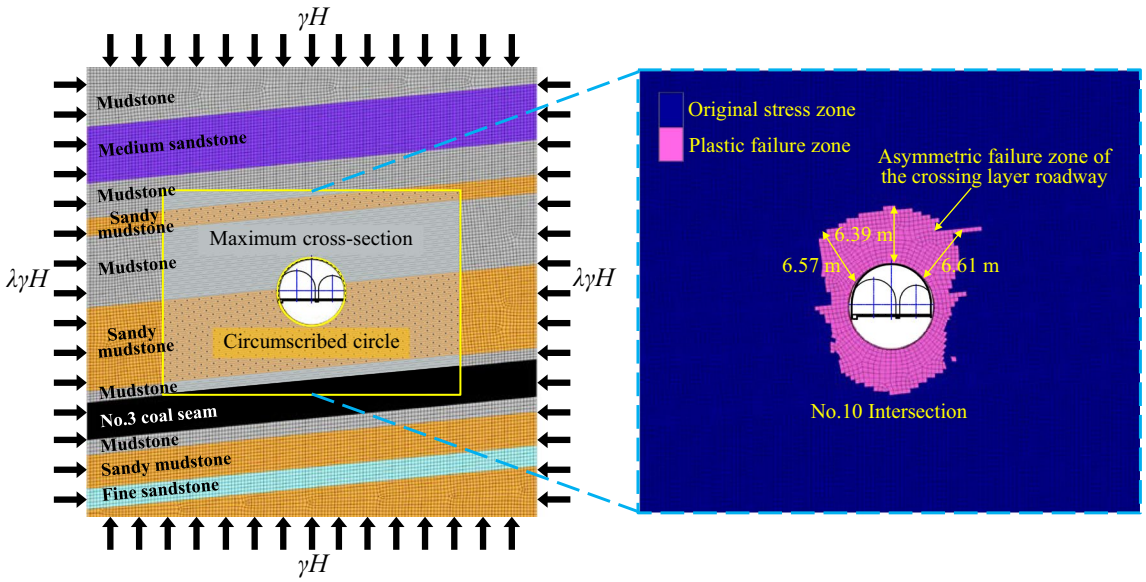

Fig. 15 Cloud map of the plastic zone at the No. 10 intersection

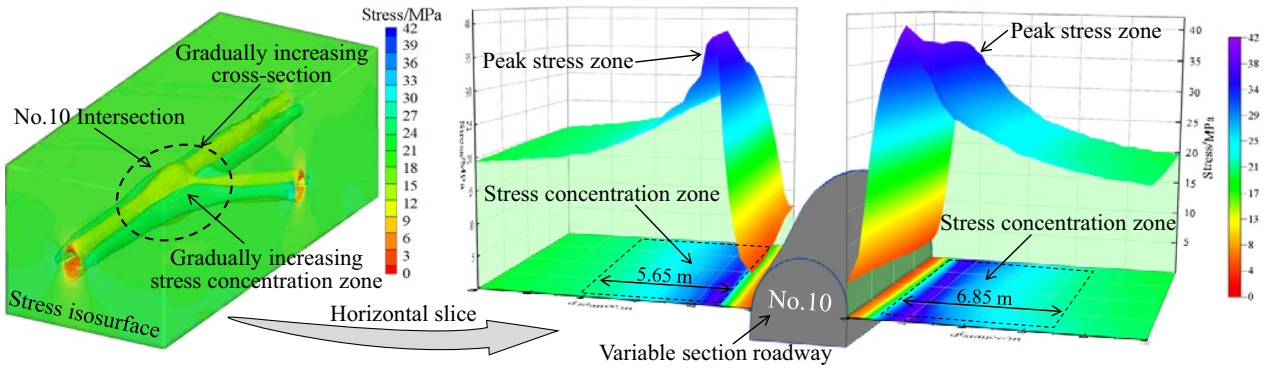

Fig. 16 Cloud map of the stress at the No. 10 intersection

combined with high-elongation anchor cables was designed, after an analysis of existing support methods, and is shown in Fig. 17a. Deep-hole grouting with grouting anchor cables was used to fill the cracks and consolidate the broken rock mass, thus changing its mechanical properties and improving its integrity (Kang et al. 2014; Li et al. 2006); the closed cracks and pores that could not be filled were compressed under the action of pressure. This correspondingly increased the deformability of rock mass. The rock mass played a significant role in compaction as it provided a reliable foundation for the anchor cables and built a thick-layered reinforced compression arch with a high bearing capacity. The strength and stability of the thick-layer reinforced compression arch bearing structure are analyzed below:

The structural mechanics model of the thick-layered reinforced compression arch is shown in Fig. 17b. P_c and P_h are the restraining resistances of the high elongation cable bolt and hollow grouting cable bolt, respectively, and P is the resultant force. The relationship between them is given by

$$\begin{cases} P_c = \dfrac{Q_c}{L_c \cdot W_c} \\ P_h = \dfrac{Q_h}{L_h \cdot W_h} \end{cases} \tag{4}$$

where Q_c and Q_h are the drawing forces of the high elongation cable bolt and hollow grouting cable bolt, respectively, and L_c, W_c, and L_h, W_h are the row and line spaces, respectively.

According to the mechanical properties of the weaker surrounding rock, the supporting rock mass follows the quadratic parabolic Mohr criterion (Li et al. 2006):

$$\tau^2 = n(\sigma + \sigma_t) \tag{5}$$

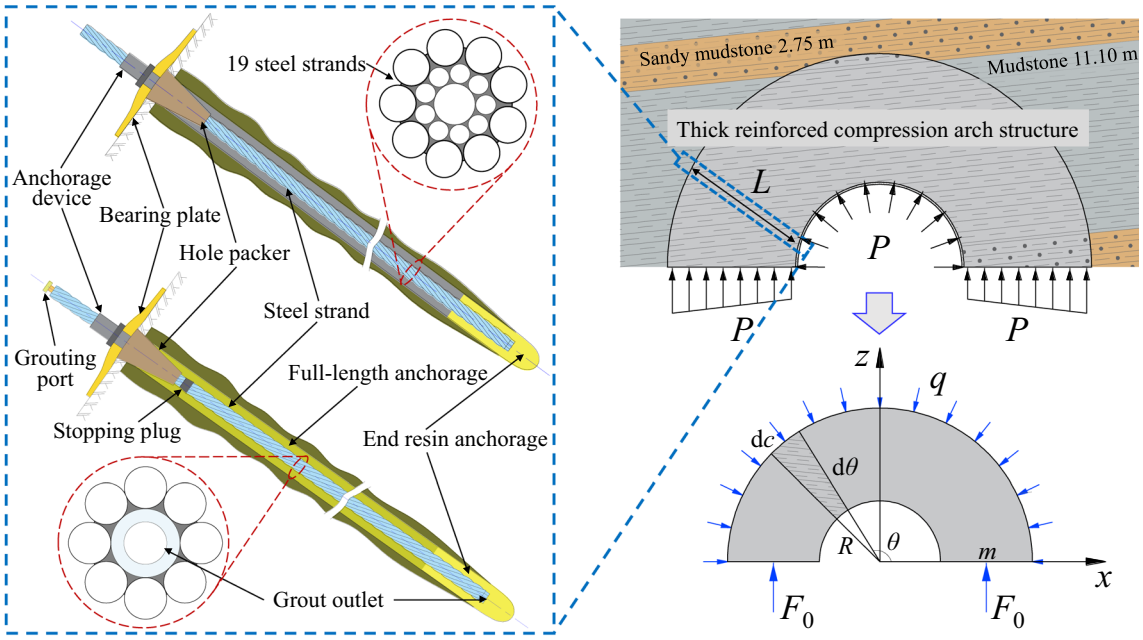

(a) Schematic of hollow grouting cable bolt and high-elongation cable bolt (b) Mechanical model

Fig. 17 Construction of thick reinforced compression arch structure

where τ is the shear strength of the supporting rock mass, σ_t is the tensile strength, and n is an undetermined coefficient.

Under the uniaxial compression test, n can be obtained by using the following formula (Li et al. 2006):

$$n = \sigma_c + 2\sigma_t \pm 2\sqrt{\sigma_t(\sigma_c + \sigma_t)} \tag{6}$$

where σ_c is the compressive strength of the supporting rock mass.

The principal stress of the quadratic parabolic envelope is expressed as:

$$(\sigma_1 - \sigma_3)^2 = 2n(\sigma_1 + \sigma_3) + 4n\sigma_t - n^2 \tag{7}$$

The stress on the inner wall of the arch structure is generally equal to the restraining force of the anchor, i.e.,

$$\sigma_3 = P \tag{8}$$

From Eqs. (7) and (8), the relation between the principal stress in the limit state and support resistance is obtained as

$$\sigma_1 = P + n + 2\sqrt{(P + \sigma_t)n} \tag{9}$$

To calculate the resultant compressive arch bearing force F per unit length along the axial direction of the roadway, the calculation principle diagram shown in the figure above was established, and the following differential equation was obtained as

$$dc = \left(R + \frac{m}{2}\right)d\theta \tag{10}$$

where dc is the differential length unit of the outer arc of the compression arch, R is the radius of the crossing roadway, m is the thickness of the backside compression arch, and $d\theta$ is the angle differential unit of the compression arch along the center of the roadway.

From Eqs. (9) and (10), the resultant compression arch bearing force F is obtained as follows:

$$F = \left(P + n + 2\sqrt{(P + \sigma_t)n}\right)b + \frac{1}{2}k^2m^2 \tag{11}$$

where k is the increasing slope of radial stress.

As anchoring is performed in fractured rock, the following relationship exists (Yu et al. 2010):

$$\begin{cases} k = 0 \\ m = \dfrac{L\tan\theta_0 - l}{\tan\theta_0} \end{cases} \tag{12}$$

where L is the average length of the bolt (cable), θ_0 is the control angle of the cable bolt in the supporting rock mass, In the curve operation of Fig. 18, the general value of θ_0 is 45° (Yu et al. 2010), and l is the row and line space between the supporting bodies. Thus, the expression for F is as follows:

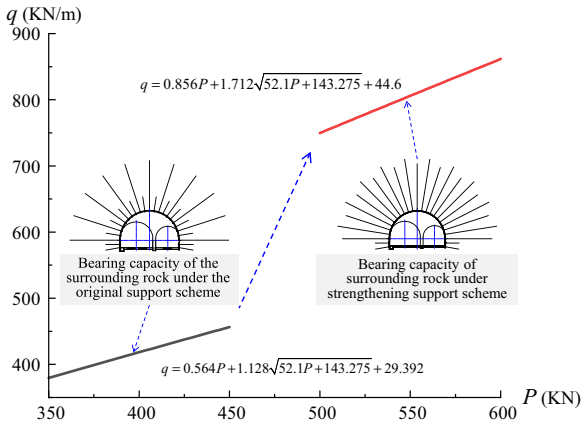

Fig. 18 Comparison of bearing capacity of compression arch under original and reinforced support schemes

$$F = \frac{L\tan\theta_0 - l}{\tan\theta_0}\left(P + n + 2\sqrt{(P+\sigma_t)n}\right) \tag{13}$$

The circular thick-layered compression arch built on the roadway is affected by the uniformly distributed load q of the deep surrounding rock. Under the action of the total support resistance P, the hoop axial force F_0 produced by the compression arch is expressed as follows:

$$2F_0 - \int_0^{\pi} q\sin\theta \cdot \mathrm{d}c = 0 \tag{14}$$

where θ is the angle between the differential element and the coordinate axis, solving the equation, we get

$$F_0 = \left(R + \frac{m}{2}\right)q \tag{15}$$

For the compression arch strength, the total bearing force F must be greater than the hoop axial force F_0 (i.e., $F \geq F_0$) to ensure stability of the structural load. When $F = F_0$, the compression arch is in the limit of the equilibrium state and the solution is given by

$$q = \frac{2\left(L\tan\theta_0 - l\right)\left(P + n + 2\sqrt{(P+\sigma_t)n}\right)}{\tan\theta_0(2R+m)} \tag{16}$$

Without considering the change in the mechanical parameters of the grouting reinforcement surrounding rock, the measured surrounding rock parameters were substituted in Eq. (16) to obtain a comparison of the bearing capacity of the compression arch formed by the original and strengthened support schemes shown in Fig. 18. It can be seen that the thick-layered reinforced compression arch formed by the reinforced support increased the support strength by 1.4 times, making the load-bearing capacity 1.8–2.3 times that of the original support, and the thickness of the load-bearing structure formed was increased by 1.76 times. Therefore, the construction of a thick-layered reinforced compression arch was achieved theoretically.

4.2 Mechanism of bolting-grouting integrated stability control

Anchor-grouting integrated stability control support technology refers to the collaborative implementation of the (1) bolt with the function of "supporting" and "pressure relief", (2) cable bolt with the function of "control" and "restriction", and (3) hollow grouting cable bolt with the function of "strengthening" and "compacting," in addition to the "filling" and "consolidation" role of the shotcrete support to achieve stability control over the large cross-section roadway at the intersection. The principle of its action is shown in Fig. 19a.

In Fig. 19b, the hollow grouting cable bolt technology is shown where the end anchors are changed to full-length anchors to improve the rigidity and shear resistance of the supporting system. Through grouting, the fractured surrounding rock was provided with high-stress radial restraint, so that the fractured rock mass could exert its stress-strengthening characteristics and provide a reliable foundation for the anchor cable. The formula for the surrounding rock reinforcement theory was derived as follows:

Uniaxial compressive strength of broken surrounding rock σ_c is given by

$$\sigma_c = \frac{2c\cdot\cos\varphi}{1-\sin\varphi} \tag{17}$$

After the process of grouting in the broken surrounding rock, there was an improvement in the cohesion c, internal friction angle φ, and elastic modulus E. The uniaxial compressive strength σ_c is given by

$$\sigma_c' = \frac{2(c+\Delta c)\cdot\cos(\varphi+\Delta\varphi)}{1-\sin(\varphi+\Delta\varphi)} \tag{18}$$

where Δc and $\Delta\varphi$ are the respective increments in the cohesion and internal friction angle, respectively. According to the Heok-Brown guidelines (Eberhardt 2012),

$$\sigma_1 = \sigma_3 + \sqrt{m\sigma_c\sigma_3 + s\sigma_c^2} \tag{19}$$

where, m and s are constants for evaluating the rock properties and integrity.

When $\sigma_1 = 0$, the uniaxial tensile strength σ_t of the rock mass is obtained as

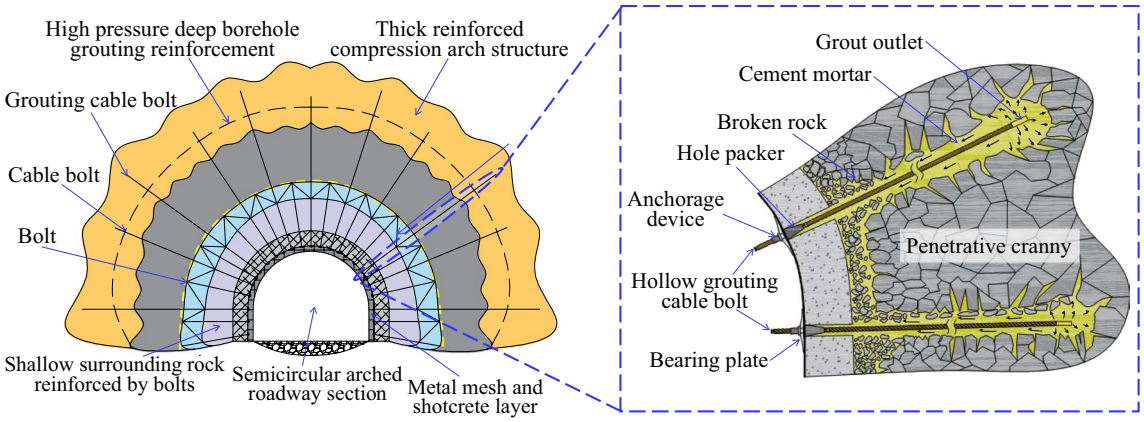

(a) Schematic of anchor-grouting integrated stability control

(b) Schematic of deep hole grouting.

Fig. 19 Principle of the role of anchor-grouting integrated stable control support

$$\sigma_t = \frac{1}{2}\sigma_c\left(m - \sqrt{m^2 + 4s}\right) \tag{20}$$

With the increase in the uniaxial compressive strength of the broken surrounding rock after grouting, the tensile strength σ_t of the strengthened surrounding rock is obtained as

$$\sigma_t' = \frac{\left(m' - \sqrt{m'^2 + 4s'}\right)(c + \Delta c) \cdot \cos(\varphi + \Delta\varphi)}{1 - \sin(\varphi + \Delta\varphi)} \tag{21}$$

where m' and s' are the rock evaluation constants after anchoring.

As shown by the strength curve in Table 3, Before the implementation of the project, the strength of rock mass specimens before and after grouting was tested in the laboratory, and the average result was that the c of rock mass increased by 2.28 MPa, an increase of 85%, and φ increased by 11°, an increase of 37%. The parameters of the mechanical properties of the surrounding rock were improved after grouting, and the values of c, φ, and E of the fissure surrounding rock increased by 66%–225%, 4°–22°, and 14%–61%, respectively (Wang et al. 2019). The analysis showed that the changes in the mechanical parameters c and φ after grouting increased the values of σ_c and σ_t significantly. From Eq. (21) it is seen that the change in the

Table 3 Change in mechanical parameters of surrounding rock after grouting

Strength curve of surrounding rock before and after grouting	Mechanical parameters	Original parameter values	Parameter increase, Δ	The increasing rate of tensile strength (%)
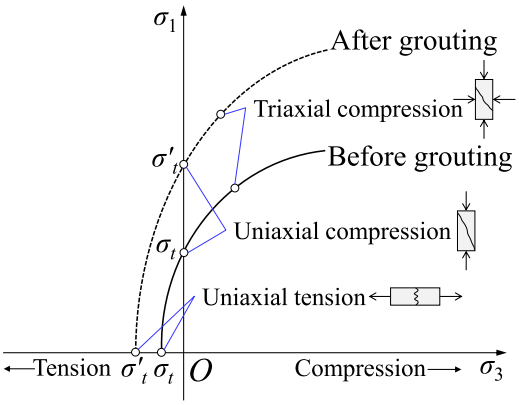	Cohesion c'	2.69 MPa	1.0 1.4 2.0 2.7	37 52 74 100
	Internal friction angle φ'	30°	5 10 15 30	11 24 39 115

values of m and s after anchoring did not produce an obvious increase in σ_t; however, when the values of c and φ increase in the same proportion, the rate of increase of σ_t is different. As shown in the above table, when the increase ratio is small, the influence of Δc on σ_t is greater, and when the increase ratio gradually increases, the influence of $\Delta\varphi$ becomes dominant.

4.3 Design of strengthening support scheme

Based on the above field test and theoretical analysis, the design strengthening support scheme of anchor network cable spray + hollow grouting cable bolt support method was adopted (Fig. 20) to ensure long-term stability of the surrounding rock of the large-section chamber in the deep well.

The specific support content was as follows: (1) The large deformed roadway under the original support was expanded and cleaned on the whole to meet the design requirements of the original Sect. (2) In accordance with the characteristics of a large cross-section and gradual cross-section at the intersection of the roadway, the design used high elongation cable bolts and hollow grouting cable bolts on the semicircular section of the roadway to be laid alternately at a 800 mm interval of the original design plan. This is because the original supporting borehole damaged the integrity of the surrounding rock and cracks around the borehole were developed, which was a key area for grouting strengthening. (3) High-strength bolts were used at the bottom corners of both sides of the roadway to strengthen the surrounding rock at the bottom corner. (4) In Fig. 20, multiple support methods combine to construct a thick-layered reinforced compression arch of over 7 m that effectively achieves roof control and reinforcement on both sides of the roadway.

4.3.1 New high-strength hollow grouting cable bolts

A new type of hollow grouting cable bolt made of high-strength spiral rib prestressed steel wire was selected for the design. Its structure and advantages of performance are shown in Fig. 21. According to previous tests, it was found that the anchoring strength increased by 15%–20%, anchoring ductility increased by approximately 25%, and the high-pressure grouting pressure could reach 8 MPa as compared with ordinary grouting anchor cables. In practice, the actual anchoring force increased by two to three times to achieve high-strength anchoring.

4.3.2 New modified cement grouting materials

As shown in Fig. 22 there are many disadvantages of cement paste in practical application, we can see that cement paste has many disadvantages when it is originally used to strengthen surrounding rock grouting, and

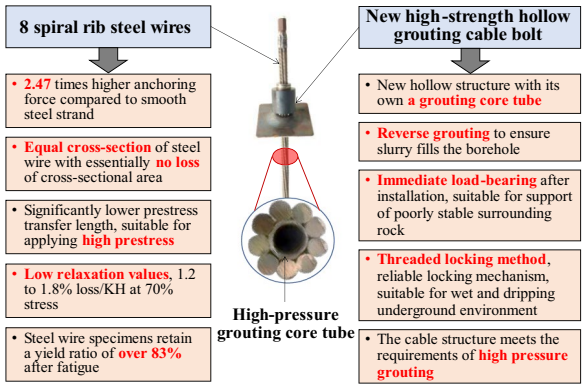

Fig. 21 New hollow grouting cable bolt made of spiral rib steel wire

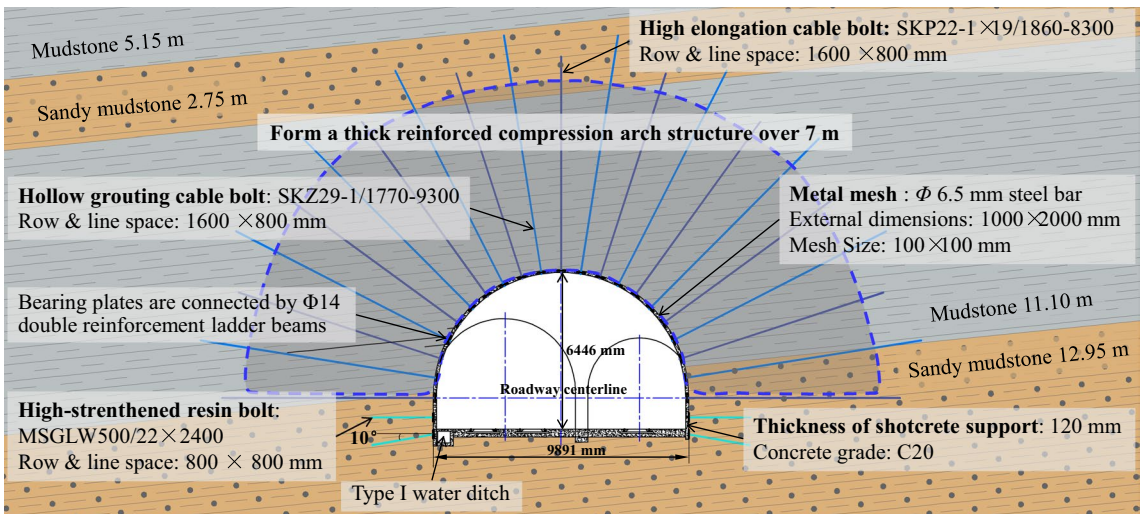

Fig. 20 Schematic of strengthening support scheme for the No. 10 intersection

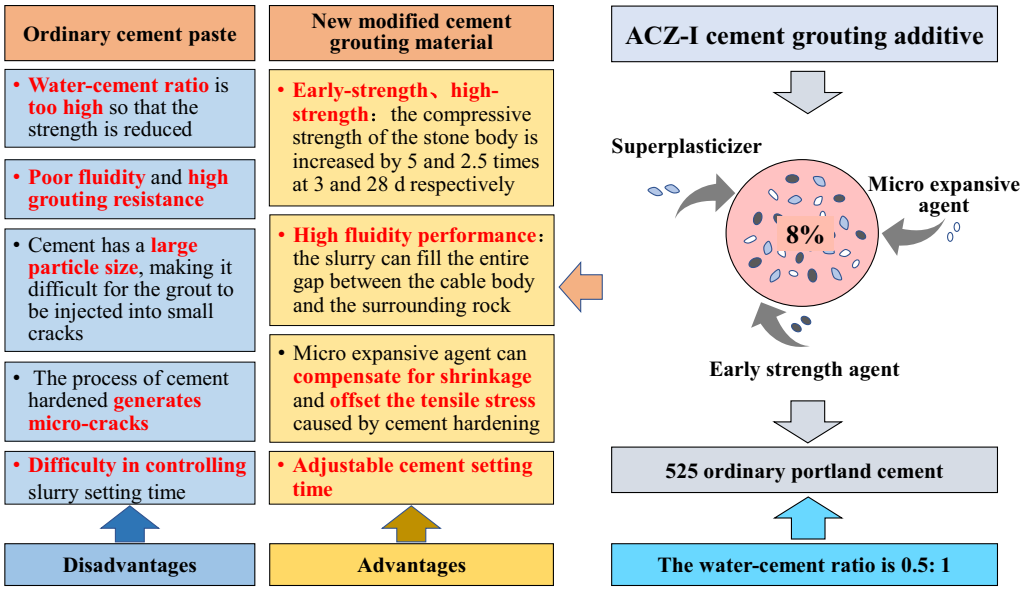

Fig. 22 Schematic of the advantages of modified grouting material

then using it combined with hollow grouting cable bolt will undoubtedly magnify these shortcomings. Therefore, a new type of grouting material which can overcome its defects should be considered to match the use of hollow grouting cable bolt. Figure 22 shows a new type of modified cement grouting material containing ACZ-I additives that contributes significantly to reducing water, plasticizing, strengthening, and micro-expansion of cement materials when grouting and strengthening surrounding rocks, thereby overcoming the current problems of high water-cement ratio, low strength, hardening shrinkage, and large pumping resistance of cement slurries. According to preliminary field testing, the pulling force of the hollow grouting cable bolt utilizing the modified cement slurry was more than twice that of ordinary paste, as shown in Table 4.

4.3.3 Selection of bolt (cable) parameters for strengthening support plan

The new high-strength hollow grouting cable bolt + high elongation cable bolt + high-strength resin bolt were used in the support design, as indicated in the Table 5 below.

4.4 Simulation analysis of supporting prestress field

4.4.1 Support model and surrounding rock compressive stress field

According to the strengthened support plan, the bolt-and-cable support system was simulated in FLAC 3D, as shown in Fig. 23, to form the surrounding rock compressive stress field (Xie et al. 2018). On examining the stress slices on the compressive stress field at the intersection, it was observed that after installation of the end of the anchor cable, a pressure of 0.02–3.00 MPa was applied to the surrounding rock of the free section and the thickness of the compressed surrounding rock was 7.24 m. From the stress cloud diagram, it is seen that the stresses of each anchor cable were cemented with each other to form a complete stress arch that improved the integrity of the surrounding rock to a great extent.

4.4.2 Prestressed field model of the integral support

Figure 24 shows the comparison of pre-stress field between original support and reinforced support. According to the prestress field formed by the original support scheme in the surrounding rock, it can be seen that the stress structure of the compressed arch can not be formed,

Table 4 Test table of pull-out force of cable bolt under different grouting materials

Grouting material	Cement paste			New modified grouting material		
Specimen number	1	2	3	4	5	6
Pull-out force (kN)	52	47	53	108	105	103

Table 5 Parameters of anchor bolt (cable) for strengthening support

Parameter	Hollow grouting cable bolt	High elongation cable bolt	High-strengthened resin bolt
Model	SKZ29-1/1770–9300	SKP22-1 × 19/1860–8300	MSGLW500/22 × 2400
Diameter (mm)	29	22	22
Length (m)	9.3	8.3	2.4
Tensile strength (MPa)	1770	1860	500
Breaking force (kN)	600	582	255
Pre-tightening force (kN)	150	200	120
Elongation	4.5%	7.0%	20.0%
Row & line space (mm)	1600 × 800	1600 × 800	800 × 800
Bearing plate (mm)	δ 20 × 300 × 300	δ 20 × 300 × 300	δ 10 × 150 × 150
Resin anchorage agent	MSK2850 × 1, MSZ2850 × 3	MSK2335 × 1, MSZ2360 × 2	MSK2335 × 1, MSZ2360 × 1
End anchorage length (m)	2.0	1.55	0.95
Others	Grouting pressure: ≥ 5.0 MPa		

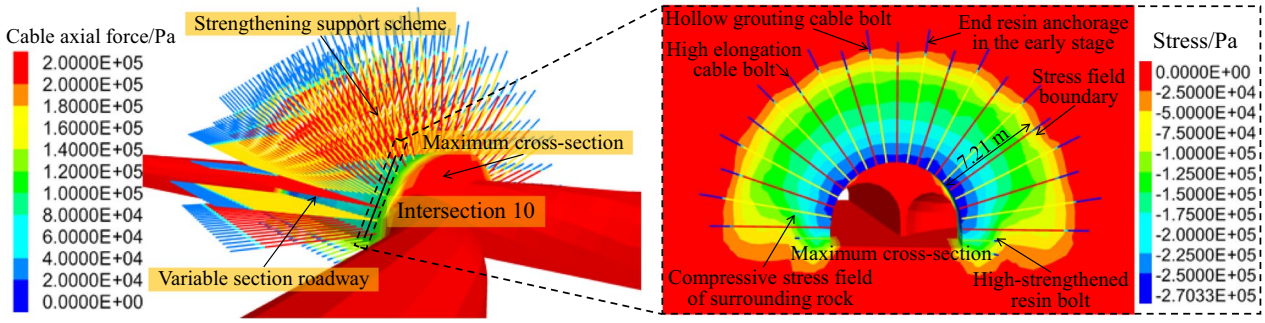

Fig. 23 Roadway supporting structure and surrounding rock compressive stress field

and there is a discontinuity between the stresses, thus becoming discontinuous. In the cloud picture of the strengthening support scheme, the stress is continuous and complete and forms a thick compressive stress arch larger than 0.02 MPa, which can act on the surrounding rock mass at a depth of more than 10 m, making the surrounding rock give full play to its self-bearing capacity, which is enough to realize the effectiveness of support and structural stability.

4.5 Construction process of strengthening support

As shown in Fig. 25 of the construction technology, the hollow grouting anchor cable construction involved more steps of installing stop plugs and grouting. When the hole or roof is broken during the drilling construction, the broken body must be put down and the drilling position cleared to facilitate the sealing and control of the drilling depth. Drilling an anchor hole must be carried out in the middle of the roof first and then the two sides from top to bottom.

5 Evaluation of effect of strengthening support

5.1 On-site implementation effect

Figure 26 shows an illustration of the field effect of the bolt-grouting support for the No. 10 crossing roadway at the bottom of the air intake shaft depot in the Nanfeng working area. After completion of the construction of the support, its functioning was under observation and the deformation was monitored for 60 days. It was found that the surrounding rock of the roadway was grouted tightly with good integrity, and there was no surface fragmentation, cracking of shotcrete layer, or slag peeling.

5.2 Deformation monitoring analysis

The convergence deformation of the surrounding rock at the No. 10 intersection was measured and the measurement curve is shown in Fig. 27. As shown in the following

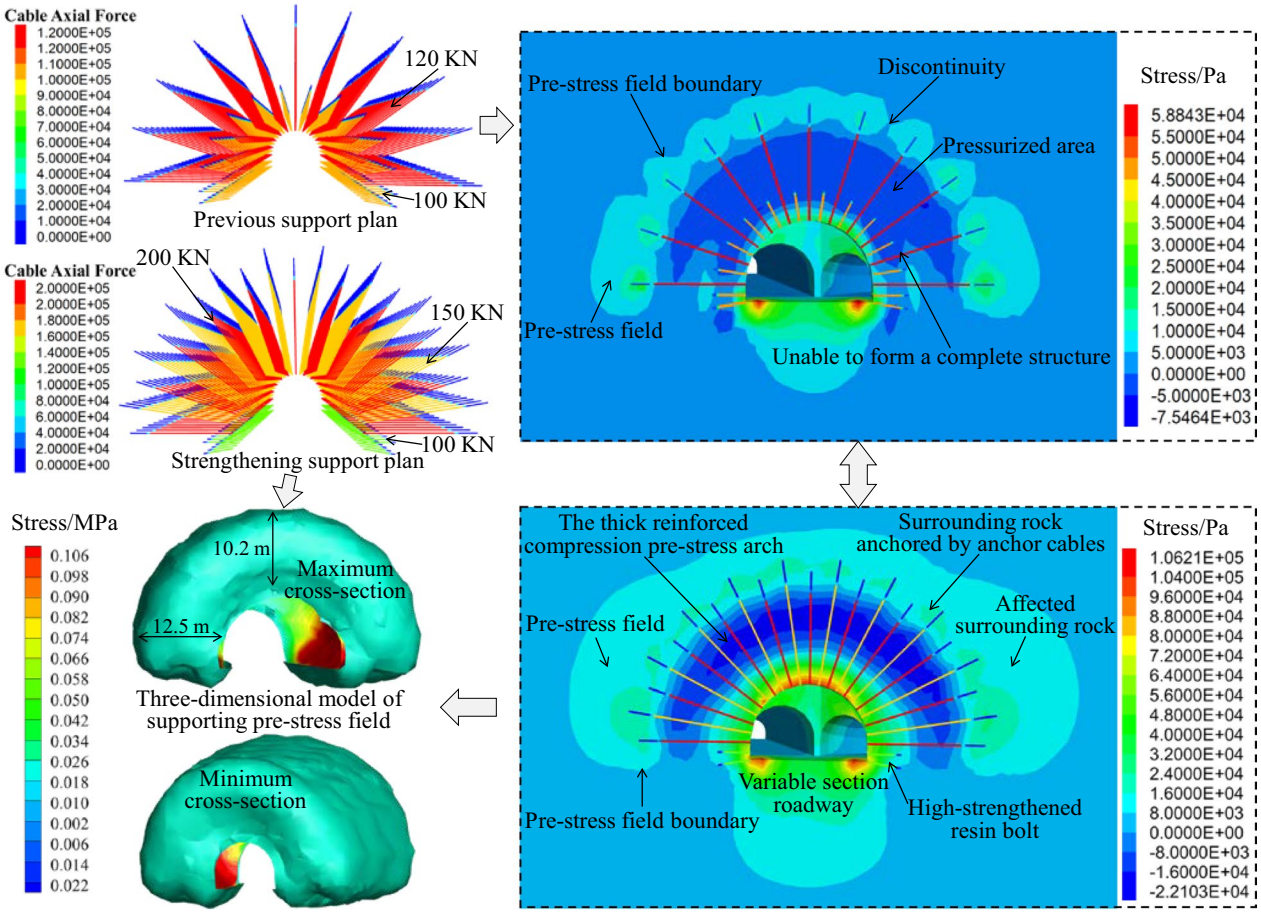

Fig. 24 Comparison of pre-stress field between original support and reinforced support

figure, the maximum convergence of the roadway is 0.4 m within 3 months after the implementation of the original support scheme, and the roof subsidence rate is fast, which has affected the normal service of the roadway. After strengthening the support, the convergence of the surrounding rock surface of the roadway is obviously small, the deformation degree of the two sides is the same as that of the floor, and the roof is the smallest. As compared with later monitoring data, the convergence deformation of the surrounding rock was faster and the rate of convergence was quite high in the first 10 days; however, it was not more than 1.5 mm/day. The rate of convergence then decreased rapidly and was approximately 0.05 mm/day for 40 days. This shows that the support form and parameters controlled the convergent deformation of the chamber effectively and maintained a relatively stable state.

5.3 Evaluation of overall effect

As shown in Fig. 28, the surrounding rock at the No. 10 intersection was assessed by drilling to evaluate the effect of the support scheme as a whole. The results showed that after carrying out the support scheme, there were cracks in the surrounding rock (0–0.4 m) in the hole. The 0.4–7.4 m rock layer was grouted and modified with good integrity, and the width of the longitudinal crack was 7.4–8.3 m. It became smaller and there were no obvious transverse cracks. The 8.3–13.4 m rock layer was fairly complete, which showed that the designed anchor-grouting integrated stability control support technology could (1) effectively control the convergence deformation of large soft rock roadway intersection in deep complex geological conditions, (2) notably reduce the roadway deformation, (3) greatly extend the period of roadway stability, (4) ensure adequate maintenance effect, and (5) generate immense economic and social benefits.

6 Conclusions

In this study, the No. 10 intersection roadway was the subject under investigation to determine the efficacy of support schemes of large-section intersection roadways surrounded by broken rock in deep formations. After on-site monitoring,

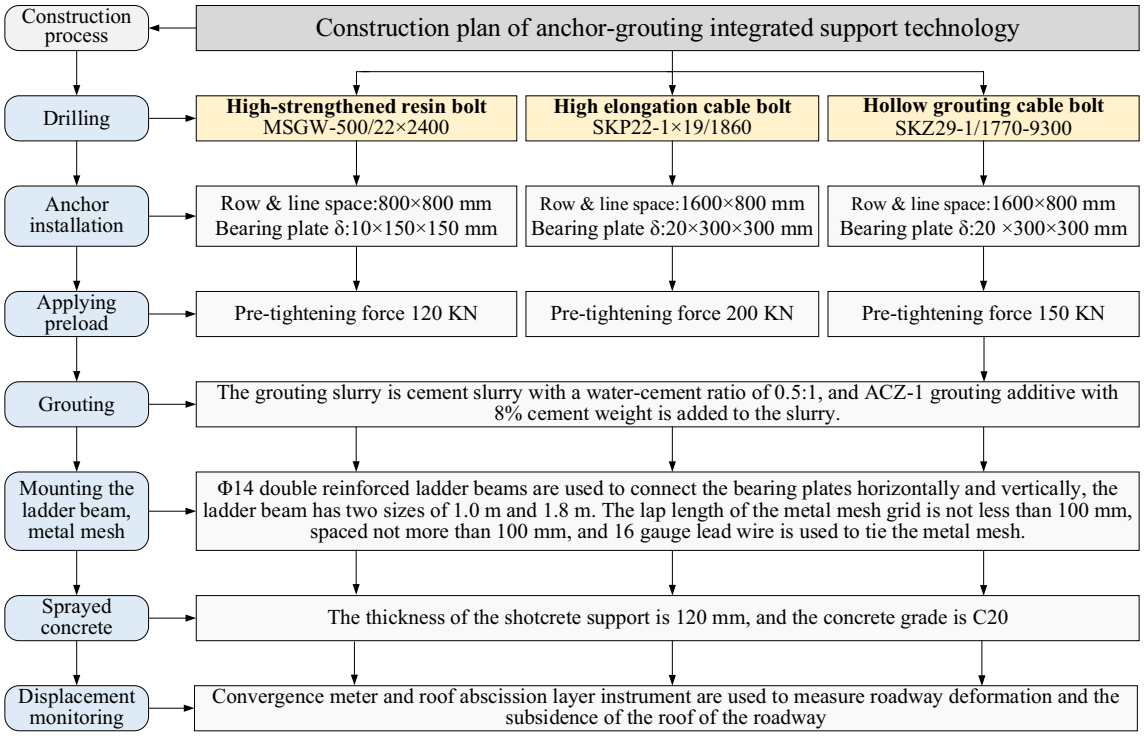

Fig. 25 Flow chart of construction of strengthening support

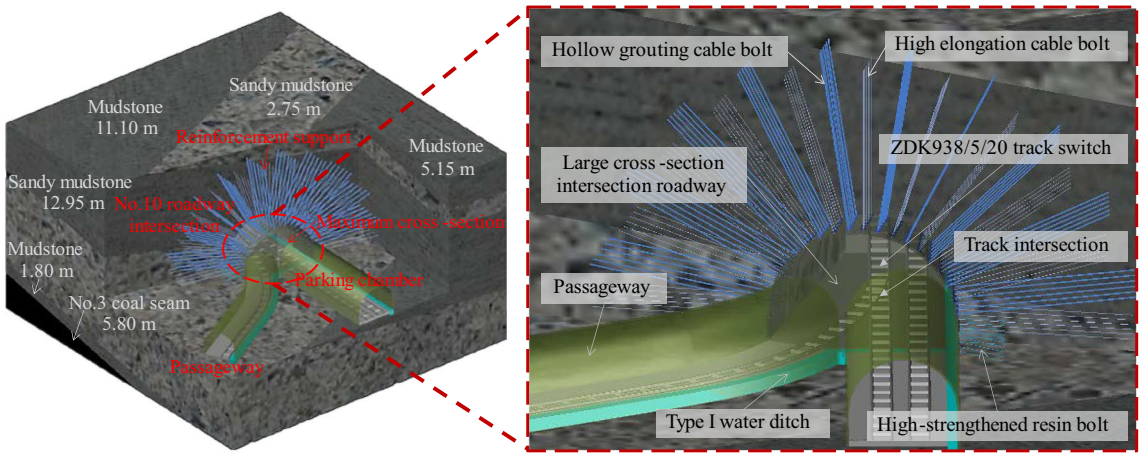

Fig. 26 Effect of strengthening support on site

theoretical analysis, numerical simulation, and construction tests, the following conclusions were drawn:

(1) With the linked reaction of variable cross-sections having a maximum width of 9.9 m, many surrounding chambers, layout under a condition of deep high stress, soft surrounding rock, adjacent faults, and cross-stratification, the intersection roadway exhibited four features, namely loose and broken surrounding rock, plastic failure zone of more than 6 m, serious destruction of roof, and high tectonic stress of nearly 30 MPa.

(2) According to the simulation of the strain-softening characteristics of the surrounding rock by FLAC 3D, the deflection of the intersection roadway increased with an increase in the size of the cross-section and the roof displacement nearly doubled in the frontal area as compared to that in the normal area. The plastic zone was deep with asymmetric distribution and had a maxi-

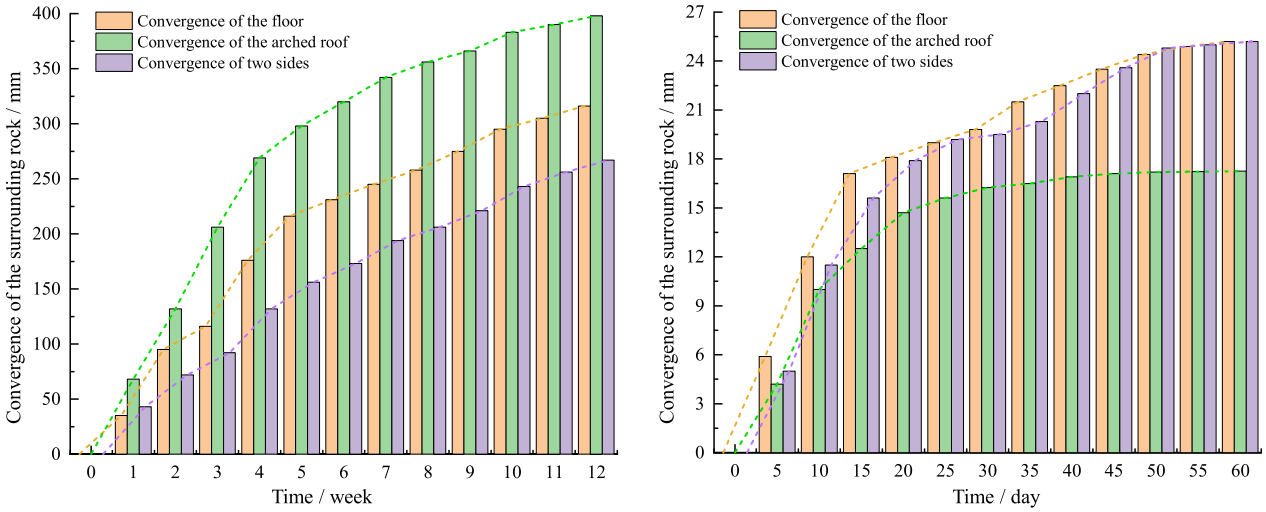

(a) Original support scheme (b) Strengthened support scheme

Fig. 27 Comparison of deformation convergence between original support and reinforced support roadway

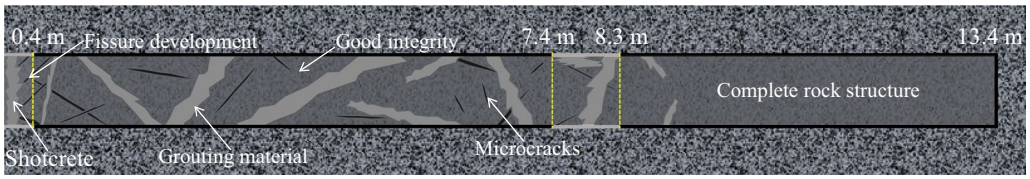

Fig. 28 Sketch drawing of borehole detection of surrounding rock after strengthening support

mum depth up to 6.61 m. It was mainly noticeable in the top and shoulder areas and disappeared gradually in the sidewall and connection between the sidewall and bottom. The stress concentration factor and range increased as compared to other areas of the roadway; they peaked at the frontal area, and the range of stress concentration at the side of the intersection roadway close to the passageway was wider and higher.

(3) In accordance with the compression arch mechanical model based on the parabolic Mohr strength theory, hollow grouting cable bolt and high elongation grouting cable bolt were utilized to build a thick strengthened compression arch more than 7 m high having a bearing capacity greater by 1.8 to 2.3 times and thickness of the bearing structure increased by 1.76 times as compared to that of the original support scheme. Thus, the construction of a large-depth, high-intensity bearing structure of the surrounding rock was accomplished successfully.

(4) According to laboratory tests, the c and φ of rock mass increased by 85% and 37% respectively after grouting. It can be calculated by the formula, an increase in the same proportion of caused a different increasing rate of σ_t, and Δc influenced σ_t to a greater extent when the proportion of increase was low; when the proportion of increase rose gradually, the influence of $\Delta\varphi$ became the leading cause of increase in σ_t.

(5) By using a modified cement grouting material and high-strength hollow grouting cable bolt, the drawing force increased to more than twice that of the cement paste; this enhanced the extent of filling of cracks and mechanical properties of the surrounding rock significantly. Based on the supporting stress field, the surrounding rock (7.24 m) was compacted and strengthened, providing a solid foundation for the attachment of the bolt (cable) support. According to the results of field monitoring, the convergence of the gallery was less than 30 mm in 60 days, indicating that stability control of the gallery was achieved effectively.

Acknowledgements This work was financially supported by the National Natural Science Foundation of China (Grant Nos. 52074296, 52004286), the China Postdoctoral Science Foundation (Grant Nos. 2020T130701, 2019M650895).

Declarations

Ethical approval The experiments comply with the current laws of China.

Conflict of interest The authors declare that they do not have any commercial or associative interest that represents a conflict of interest in connection with the work submitted.

References

Alonso E, Alejano LR, Varas F, Fdez-Manin G, Carranza-Torres C (2003) Ground response curves for rock masses exhibiting strain-softening behaviour. Int J Numer Anal Methods Geomech 27(13):1153–1185

Cai MF, Brown ET (2017) Challenges in the mining and utilization of deep mineral resources. Engineering 3(4):432–433

Chen XJ, Li LY, Wang L, Qi LL (2019) The current situation and prevention and control countermeasures for typical dynamic disasters in kilometer-deep mines in China. Saf Sci 115:229–236

Eberhardt E (2012) The Hoek-Brown failure criterion. Rock Mech Rock Eng 45(6):981–988

Fairhurst C (2017) Some challenges of deep mining. Engineering 3(4):527–537

Huang X, Liu QS, Liu B, Liu KD, Huang SB (2014) Experimental research on the mechanical behavior of deep soft surrounding rock tunneling by TBM. J China Coal Soc 39(10):1977–1986 ((**in Chinese**))

Huang J, Zhang YM, Zhu LS, Wang T (2016) Numerical simulation of rock cutting in deep mining conditions. Int J Rock Mech Min Sci 84:80–86

Huang WP, Yuan Q, Tan YL, Wang J, Liu GL, Qu GL, Li C (2018) An innovative support technology employing a concrete-filled steel tubular structure for a 1000-m-deep roadway in a high in situ stress field. Tunn Undergr Space Technol 73:26–36

Kang YS, Liu QS, Gong GQ, Wang HC (2014) Application of a combined support system to the weak floor reinforcement in deep underground coal mine. Int J Min Sci Technol 71:143–150

Kang HP, Lin J, Fan MJ (2015) Investigation on support pattern of a coal mine roadway within soft rocks — a case study. Int J Coal Geol 140:31–40

Kawamoto T, Ishizuka Y (1981) An analysis of excavation instrain-softening rock mass. Proc Japan Soc Civ Eng 148:107–118

Lee YK, Pietruszczak S (2008) A new numerical procedure for elasto-plastic analysis of a circular opening excavated in a strain-softening rock mass. Tunn Undergr Space Technol 23(5):588–599

Li CG, Ge XR, Zheng H, Wang SL (2006) Two-parameter parabolic Mohr strength criterion and its damage regularity. Key Eng Mater 306–308:327–332

Li XF, Wang SB, Malekian R, Hao SQ, Li ZX (2016) Numerical simulation of rock breakage modes under confining pressures in deep mining: an experimental investigation. IEEE Access 4:5710–5720

Li G, Ma FS, Guo J, Zhao HJ, Liu G (2020) Study on deformation failure mechanism and support technology of deep soft rock roadway. Eng Geol 264:105262

Liu CR (2011) Distribution laws of in-situ stress in deep underground coal mines. Procedia Eng 26:909–917

Lu YL, Wang LG, Yang F, Li YJ, Chen HM (2010) Post-peak strain softening mechanical properties of weak rock. Chin J Rock Mech Eng 29(3):640–648 ((**in Chinese**))

Pan R, Wang Q, Jiang B, Li SC, Sun HB, Qin Q, Yu HC, Lu W (2017) Failure of bolt support and experimental study on the parameters of bolt-grouting for supporting the roadways in deep coal seam. Eng Fail Anal 80:218–233

Peng R, Meng X, Zhao G, Li Y, Zhu J (2018) Experimental research on the structural instability mechanism and the effect of multi-echelon support of deep roadways in a kilometre-deep well. PLoS One 13(2):e0192470

Ranjith PG, Zhao J, Ju MH, De Silva Radhika VS, Rathnaweera TD, Bandara AKMS (2017) Opportunities and challenges in deep mining: a brief review. Engineering 3(4):546–551

Shreedharan S, Kulatilake PHSW (2015) Discontinuum–equivalent continuum analysis of the stability of tunnels in a deep coal mine using the distinct element method. Rock Mech Rock Eng 49(5):1903–1922

Tan YL, Fan DY, Liu XS, Song SL, Li XF, Wang HL (2019) Numerical investigation of failure evolution for the surrounding rock of a super-large section chamber group in a deep coal mine. Energy Sci Eng 7(6):3124–3146

Tian ZC, Tang CA, Liu YJ, Tang YB (2020) Zonal disintegration test of deep tunnel under plane strain conditions. Int J Coal Sci Technol 7(2):337–349. https://doi.org/10.1007/s40789-020-00319-y

Wagner H (2019) Deep mining: a rock engineering challenge. Eng Mech Rock Eng 52(5):1417–1446

Wang MY, Zhang N, Li J, Ma LJ, Fan PX (2015) Computational method of large deformation and its application in deep mining tunnel. Tunn Undergr Space Technol 50:47–53

Wang Q, Pan R, Jiang B, Li SC, He MC, Sun HB, Wang L, Qin Q, Yu HC, Luan YC (2017) Study on failure mechanism of roadway with soft rock in deep coal mine and confined concrete support system. Eng Fail Anal 81:155–177

Wang Q, Qin Q, Jiang B, Yu HC, Pan R, Li SC (2019) Study and engineering application on the bolt-grouting reinforcement effect in underground engineering with fractured surrounding rock. Tunn Undergr Space Technol 84:237–247

Wang H, Jiang C, Zheng PQ, Li N, Zhan YB (2020) Deformation and failure mechanism of surrounding rocks in crossed-roadway and its support strategy. Eng Fail Anal 116:104734

Xie HP, Gao MZ, Zhang R, Peng GY, Wang WY, Li AQ (2018) Study on the mechanical properties and mechanical response of coal mining at 1000m or deeper. Rock Mech Rock Eng 52(5):1475–1490

Xie S, Mingming G, Dongdong C, Yanding,S, Hao P, Hai S, Shizhong L (2018) Stability influence factors analysis and construction of a deep beam anchorage structure in roadway roof. Int J Min Sci Technol 28(3):445-451. https://doi.org/10.1016/j.ijmst.2017.11.007

Xie SR, Pan H, Zeng JC, Wang E, Chen DD, Zhang T, Peng XJ, Yang JH, Chen F, Qiao SX (2019) A case study on control technology of surrounding rock of a large section chamber under a 1200-m deep goaf in Xingdong coal mine, China. Eng Fail Anal 104:112–125

Xue D, Zhou J, Liu Y, Gao L (2020) On the excavation-induced stress drop in damaged coal considering a coupled yield and failure criterion. Int J Coal Sci Technol 7(1):58–67

Yang SQ, Chen M, Jing HW, Chen KF, Meng B (2017) A case study on large deformation failure mechanism of deep soft rock roadway in Xin'An coal mine, China. Eng Geol 217:89–101

Yao YM, Neithalath N, Mobasher B (2018) Analysis and design procedures for strain hardening flexural beam and panel. RILEM Bookseries 15:518–526

Yu WJ, Gao Q, Zhu CQ (2010) Study of strength theory and application of overlap arch bearing body for deep soft surrounding rock. Chinese J Rock Mech Eng 29(10):2134–2142 ((**in Chinese**))

Yu KP, Ren FY, Puscasu R, Lin P, Meng QG (2020) Optimization of combined support in soft-rock roadway. Tunn Undergr Space Technol 103:103502

Zhang F, Sheng Q, Zhu ZQ, Zhang YH (2008) Study on post-peak mechanical beha viour and strain-softening model of three gorges granite. Chin J Rock Mech Eng 27(S1):2651–2655 ((**in Chinese**))

Zhang HQ, Miao XX, Zhang GM, Wu Y, Chen YL (2017) Non-destructive testing and pre-warning analysis on the quality of bolt support in deep roadways of mining districts. Int J Min Sci Technol 27(6):989–998

Zhang JP, Liu LM, Cao JZ, Yan X, Zhang FT (2018) Mechanism and application of concrete-filled steel tubular support in deep and high stress roadway. Constr Build Mater 186:233–246

Zhang CY, Pu CZ, Cao RH, Jiang TT, Huang G (2019) The stability and roof-support optimization of roadways passing through unfavorable geological bodies using advanced detection and monitoring methods, among others, in the Sanmenxia Bauxite Mine in China's Henan Province. Bull Eng Geol Environ 78(7):5087–5099